Enhanced efficiency and environmental stability of planar perovskite solar cells by suppressing photocatalytic decomposition

Journal:	*Journal of Materials Chemistry A*
Manuscript ID	TA-ART-05-2017-004014.R1
Article Type:	Paper
Date Submitted by the Author:	01-Jul-2017
Complete List of Authors:	Zhang, Peng; University of Electronic Science and technology of China, Wu, Jiang; University of Arkansas, ; University College London, Wang, Yafei; School of Optoelectronic Information, University of Electronic Science and Technology of China (UESTC), Sarvari, Hojjatollah; University of Kentucky; University of Kentucky Liu, Detao; University of Electronic Science and technology of China Chen, Zhi; School of Optoelectronic Information, University of Electronic Science and Technology of China (UESTC); University of Kentucky, Lexington, Kentucky 40506 Li, Shibin; School of Optoelectronic Information, University of Electronic Science and Technology of China (UESTC),

Enhanced efficiency and environmental stability of planar perovskite solar cells by suppressing photocatalytic decomposition

Peng Zhang[1], Jiang Wu[2], Yafei Wang[1], Hojjatollah Sarvari[3], Detao Liu[1], Zhi David Chen[1,3,*] & Shibin Li[1,*]

1 School of Optoelectronic Information, University of Electronic Science and Technology of China, Chengdu 610054, China.

2 Department of Electronic and Electrical Engineering, University College London, Torrington Place, London WC1E7JE, UK.

3 Department of Electrical & Computer Engineering and Center for Nanoscale Science & Engineering, University of Kentucky, Lexington, Kentucky 40506, USA.

---

[*] Address correspondence to Shibin Li, shibinli@uestc.edu.cn; Zhi David Chen, zhichen@engr.uky.edu

ABSTRACT

The environmental instability of perovskite solar cells caused by the ultraviolet photocatalytic effect of metal oxide layers is a critical issue that must be solved. In this paper, we report improved environmental stability of ZnO film based planar heterojunction perovskite solar cells, by suppressing photocatalytic activities induced by the ZnO electron transfer layer. The photovoltaic performance and stability in an ambient environment under continuous illumination are effectively improved by applying an aluminum oxide interlayer on the ZnO film to suppress the photocatalytic degradation of perovskites. The highest efficiency of solar cells has increased from 14.62% to 17.17%, and after 250 h continuous exposure under full spectrum simulated sunlight in air, the efficiency remains as high as 15.03%. The results suggest that effective suppressing of photocatalytic degradation of perovskites with a modified electron transfer layer is a new solution to improve the long term environmental stability of perovskite solar cells.

1. Introduction

The organometal trihalide perovskite materials have attracted great attention over the past few years because of their outstanding photovoltaic properties. In 2009, Kojima et al. developed the first perovskite solar cell (PSC), while they only gained a power conversion efficiency (PCE) of 3.8%.[1] Following their research, a series of methods, such as sequential deposition method,[2-6] one step method,[7-9] solvent engineering,[10,11] anti-solvent method,[11-13] vapor deposition etc. have been developed to improve the quality of perovskite films, leading to a drastic increase of PCEs.[14,15] In addition to the improved fabrication methods, new perovskite compounds such as $FA_{1-x}MA_xPb(I_{1-y}Br_y)_3$,[4,16-19] $FAPbI_X$,[20,21] $CsPbX_3$ etc.,[22-24] where FA = formamidinium, MA = methylamomnium, X = Cl, Br, I, were used to replace the original $MAPbI_3$, and the PCEs of PSCs were further improved. Up to now, the highest PCE of PSCs based on TiO_2 has surged to remarkably 21.1%.[25]

Taking advantage of a high electron mobility (205-300 cm^2/Vs for bulk ZnO).[26,27] ZnO appears to be a competitive alternative to TiO_2 (0.1-4 cm^2/vs) as the electron transport material (ETM) for PSCs.[28] In addition, ZnO with various micro structures can be produced using many simple methods at low temperature.[29,30] The first ZnO nanorod based perovskite solar cells reported in 2013 showed a PCE of 5% owing to the limitation of using a traditional DSSC structure.[31] By replacing the surface sensitization structure with a heterojunction structure, Son et al. fabricated a ZnO nanorod based bulk heterojunction PSC with a PCE of 11.13%.[32] Planar heterojunction PSCs with low temperature processed thin ZnO nanoparticle films prepared by Liu et al. showed a PCE of 15.7%.[30] Furthermore, Mahmood et al. increased the PCE of PSCs to 16.1% by using polyethyleneimine (PEI) modified nitrogen doped ZnO nanorods as the ETM.[33] Our previous study also showed a record high efficiency of PSCs based on

ZnO nanorods exceeding 17% by passivation of the ZnO ETM with atomic layer deposition of Al_2O_3.[34,35] Recently, Tseng et al. reported the first Al-doped ZnO (AZO) based planar heterojunction PSC with the highest PCE of 17.6%.[36]

The rapid development of ZnO based PSCs shows the great potential of ZnO as the ETM, but the efficiency and stability of ZnO based PSCs are still inferior to those of TiO_2 based PSCs. The low PCE of ZnO based PSCs is mainly owing to serious charge recombination at the interface between the ZnO nanostructure and perovskite.[37] Surface passivation is an efficient method to solve this problem.[33,34,37] On the other hand, the poor long term stability also severely limits the performance of ZnO based PSCs. This instability includes two aspects: thermal decomposition and ultraviolet (UV) degradation. The thermal decomposition process has been extensively studied, and many methods have been used to overcome this problem.[38-40] However, compared with the widely studied thermal decomposition, the studies on UV degradation are still insufficient. UV degradation is a common problem for both ZnO and TiO_2 based PSCs. In 2013, Leijtens et al. reported the UV degradation phenomenon in TiO_2 based PSCs.[41] They found that photocatalysis of TiO_2 rapidly degrades the performance of PSCs after long-time illumination. By replacing the UV sensitive TiO_2 with Al_2O_3, PSCs with high stability were obtained. The UV degradation was also restrained by using defective TiO_2 and CsBr surface modification.[42,43] The UV degradation of ZnO based PSCs is more severe than that of TiO_2 based PSCs because of the stronger UV catalytic activity of ZnO. Surface hydroxyl groups and chemical residues left over on the solution processed ZnO surface cause photochemical reaction and accelerate the decomposition of perovskite.[44,45] Hence, there is an urgent need to enhance the UV resistance of ZnO based PSCs.

In this paper, we report the first direct evidence (Fourier Transform Infrared

Spectroscopy, FTIR) for effective suppression of photocatalytic decomposition of $MAPbI_3$ in efficient planar PSCs based on undoped ZnO film. Using a ZnO ETM modified by an ultrathin AlO_x interlayer (marked as Al-ZnO), the solar cell efficiency has been improved from 14.62% of a control device using the bare ZnO (marked as RF-ZnO) to a high PCE of 17.17%. In addition, the ultrathin AlO_x interlayer effectively inhibits ZnO-assisted photocatalytic reactions in PSCs. After 250 h full spectrum solar illumination in ambient air, the PCE slightly decreased to 15.03%, representing the long life time of ZnO based PSCs. The FTIR spectroscopy and dark current results obtained from different aging stages confirmed that the AlO_x interlayer not only passivates the ZnO surface but also improves the environmental stability by suppressing the ZnO-assisted photocatalysis of perovskites.

2. Materials and Methods

2.1 Materials.

PbI_2, CH_3NH_3I and the all other chemicals were purchased from Sigma-Aldrich Co. and used as received.

2.2 Device preparation.

Patterned FTO glasses were cleaned sequentially by detergent, acetone, ethanol and DI water in ultrasonic bath before use.

A compact 20 nm ZnO film was deposited on FTO by RF sputtering with a ZnO target. To prepare the ZnO film with AlO_X interlayer (Al-ZnO), 1-2 nm Al film was deposited on the compact ZnO by E-beam evaporation system, and due to the low reduction potential of Al and the ultrathin layer thickness, the Al film was oxidized and formed an ultrathin AlO_X interlayer on the ZnO surface once the film was exposed to air. Solution containing ZnO nanoparticles was also employed to prepare ZnO film (S-ZnO) by a spin coating process.[30]

The samples were then transferred to N_2 filled glove box to deposit perovskite films ($MAPbI_3$) using the single step method.[47] Precursor solution was prepared by using 78 mg DMSO and 600 mg DMF to completely dissolve 461 mg PbI_2 and 159 mg CH_3NH_3I (MAI). The prepared solution was spin-coated on the ZnO surface at 4000 rpm for 25 s, and 0.5 ml of chlorobenzene was dropped on the film surface in 15 s before the end of spin coating process. The sample was then annealed at 65 ^{o}C for 1 min and 100 ^{o}C for 2 min. After cooling down to room temperature, hole transport material (spiro-OMeTAD solution with additional of TBP, Li-TFSI and Co salt) was spin coated on the $MAPbI_3$ surface.[2] Finally, a 60 nm Au metal electrode was deposited by thermal evaporation. The active area for all solar cells was 0.09 cm^2.

To examine the defect concentration in perovskite films, electron-only devices were fabricated. The electron-only devices are consisted of FTO/ZnO/$MAPbI_3$/PCBM/Ag. To fabricate the electron only devices, after the perovskite layer was prepared, a 20 nm [6,6]-phenyl-C61-butyric acid methyl ester (PCBM) layer was spin coated on the $MAPbI_3$ surface, the precursor solution was made by dissolving 20 mg PCBM in 1 ml chlorobenzene. A 50 nm Ag film was deposited as an electrode by thermal evaporation.

2.3 Measurement and Characterization.

Current-voltage characteristics were recorded by Keithley 2400 under AM 1.5G illuminations (100 mW/cm^2) from a solar simulator (Newport Oriel Solar 3A Class AAA, 64023A). The AM 1.5G sun light was calibrated by standard Si-solar cell (Oriel, VLSI standards).

The external quantum efficiency (EQE) measurements were performed employing a solar cell quantum efficiency measurement system (QEX10, made by PV Measurements, USA) with a dual grating monochromator with computer control.

XRD tests were carried out using a Bede D1 system with Cu Kα radiation. The surface and cross section morphology were obtained from field emission fitting SEM (FEI-Inspect F50, Holland). The UV-Vis absorption spectrum was measured by an UV-Vis spectrophotometer (Schimadzu UV-3101 PC). FTIR spectrum was obtained from Fourier transform infrared spectroscopy (FTIR, Nicolet 6700, Thermo Scientific). The XPS was measured using the Kratos XSAM 800 X-Ray Photoelectron Spectrometer.

Photoluminescence (PL) was measured by the F-4600 FL fluorescence spectrophotometer. Time-resolved photoluminescence (TRPL) spectra of the samples were measured using a Fluorolog-3 fluorescence spectrophotometer. For PL and TRPL tests, samples with structures of FTO/ZnO(RF sputtering)/Al/Perovskite (for Al-ZnO), FTO/ZnO(RF sputtering)/Perovskite (for RF-ZnO) and FTO/ZnO(solution process)/Perovskite (for S-ZnO) were prepared.

To examine the UV degradation process, the PSCs without encapsulation were illuminated by AM 1.5G sunlight from a solar simulator (Newport Oriel Solar 3A Class AAA, 64023A) under room temperature in air (25 ^{o}C, 30%RH). Air flow was used to maintain the devices' temperature. The exposure time was 250 h.

To study photocatalytic activity, 5mg/L of aqueous methylene blue (MB) solution was used in the presence of different ZnO films under the UV illumination at room temperature. A 4 cm^2 ZnO film was immersed in 10 ml MB solution. Before irradiation, solution was magnetically stirred in dark for 30 min to achieve adsorption equilibrium. In degradation process, the solutions were irradiated from top with a UV light (360 nm, 25 W) and stirred during the whole process. The concentration of MB solution was determined by the UV-Vis spectrometer every 20 min.

3. Result and Discussion

Fig. 1(a) shows the diagram of PSCs after AlO_x interlayer modification, the energy level diagram of FTO/ZnO(Al)MAPbI$_3$/spiro-OMeTAD is shown in the inset.[45-47] As shown in Fig. S1, the AlO$_x$ interlayer hardly affects the optical transmittance. To study the degradation of PSCs caused by UV light, we exposed a number of PSCs to full spectrum AM 1.5G simulated sunlight (100 mW/cm^2). As a control sample, a PSC based on sol-gel ZnO film is also prepared (marked as S-ZnO).

Fig. 1(b) exhibits the J-V curves of the best performing PSCs based on RF-ZnO and Al-ZnO before UV illumination, the J-V curve of PSC based on S-ZnO is shown in Fig. S2(a). The device based on S-ZnO shows the lowest PCE of 9.2%, with FF = 60%, V_{OC} = 1.06 V, J_{SC} = 14.4 mA/cm^2. By using RF-ZnO film as ETM, the PCE of device increases to 14.62%, with FF of 68.25%, V_{OC} of 1.05 V and J_{SC} of 20.4 mA/cm^2. The use of AlO$_x$ interlayer further increases the PCE to 17.17%, with FF of 75.9%, V_{OC} of 1.053 V and J_{SC} of 21.55 mA/cm^2.

Fig. 1(c) shows the external quantum efficiency (EQE) spectra of best performing PSCs based on Al-ZnO and RF-ZnO. Both curves show a strong light response in the range from 350 nm to 700 nm. For PSC based on RF-ZnO, the spectrum intensity decreases slightly in the range from 500 nm to 700 nm. As for S-ZnO, the EQE spectrum is shown in Fig. S2(b). Compared with the spectra of PSCs based on Al-ZnO and RF-ZnO, the whole spectrum intensity of PSC based on S-ZnO decreased significantly. The differences between EQE spectra of Al-ZnO, RF-ZnO and S-ZnO mainly come from the different properties of MAPbI$_3$ films and the interface between ZnO surface and perovskite film, which will be explained in detail later. In addition, the J_{SC} of PSC based on Al-ZnO calculated from the EQE data is 21 mA/cm^2, and for PSC based on Al-ZnO and S-ZnO, the calculated J_{SC} are 20.1 mA/cm^2 and 14.4 mA/cm^2 respectively, which are in good agreement with the measured results from J-V test.

In addition, the J-V curves of best performance PSC based on Al-ZnO measured by forward and reverse scans are shown in Fig. S3. As can be seen from the figure, a PCE of 16.93% was obtained from forward scan and a PCE of 17.17% was obtained from reverse scan, which shows a small hysteresis between the reverse and forward scan. This can be attributed to the effective improvement of the crystallinity and grain size of $MAPbI_3$ films and the modified interface between $MAPbI_3$ and ZnO. Fig. S4 shows steady state photocurrent output of the best performing PSC based on Al-ZnO. The stable current density measured at the maximum power point at 0.82V is 20.8 mA/cm^2, which is in good agreement with the measured result. And the stable PCE corresponding to this current density is 17.05%, which represents the actual power output and efficiency.

Fig. 1(d) shows the performance deterioration of planar PSCs based on Al-ZnO and RF-ZnO over 250 h continuous illumination under full spectrum solar simulator in air (30% relative humidity (RH), 25 ^oC). The PSCs based on Al-ZnO films showed improved stability under UV exposure, and the PCE had minor decrease from 17.17% to 15.03% after aging test. Other photovoltaic parameters, especially the J_{sc}, degraded slightly. However, the performance of PSCs based on RF-ZnO degraded drastically. The PCE decreased from 14.62% to 7.07% after 250 h illumination. As shown in Fig. S5, solar cells based on S-ZnO show even poorer stability. Complete device failure is observed in the first few hours of aging test. The detailed photovoltaic data of these solar cells are shown in Table S1. According to the results, the PSCs based on Al-ZnO and RF-ZnO showed much better initial performance and stability than PSCs with S-ZnO. The poor performance of S-ZnO device mainly came from a high defect density of the ZnO film because of the incompletely conversion of Zn precursors to ZnO during the solution process.[44] The poor stability should be attributed to the much stronger photocatalysis activity of S-ZnO. Thus, by replacing the solution process with RF sputtering, the ZnO material properties were improved. With AlO_x interlayer modification, the surface recombination of RF-ZnO was further suppressed. Therefore, the RF-ZnO and Al-ZnO devices showed better performance than the S-ZnO device.

To further investigate the degradation mechanism of PSCs based on different ZnO materials, we carried out an UV aging test. The UV aging test was carried out by illuminating the unencapsulated PSCs with sunlight from a solar simulator (contain about 4.6 mW/cm^2 of UV light less than 400 nm in the spectrum) under room temperature in air (25 ^oC, 30%RH).[43] The exposure time was 250 h and cool air flow was used to maintain the temperature of samples. In addition, according to previous reports, the visible light (> 400 nm) cannot fully stimulate the photocatalysis of ZnO under common condition. Furthermore, according to the researches of Leijtens et al. and Li et al., the $MAPbI_3$ itself can remain stable under visible light.[41, 43] As a result, no filter was used during the aging process. The FTIR analysis was used to monitor the evolution of $MAPbI_3$ during the UV aging processes. Per the results reported by Antonio Abate et al, the commonly considered unstable spiro-OMeTAD can maintain stability once the oxidation reaction is complete.[49] Thus, the degradation of PSCs performance is mainly attributed to the UV light induced photochemical reaction at the interface between ZnO and $MAPbI_3$.

As shown in Fig. 2(a), FTIR spectra suggest the improved UV stability of $MAPbI_3$ film on Al-ZnO. All the samples obviously show N-H stretching and C-H stretching vibration at around 3250 cm^{-1} and 2987 cm^{-1}, which can be attributed to the $CH_3NH_3^+$ radical in $MAPbI_3$ film. The C-N stretch and C-H bend, which correspond to MA cations in the $MAPbI_3$ film, are also observed. The light illumination causes marginal changes in the FTIR spectra of the $MAPbI_3$ film on Al-ZnO. However, all the vibration modes in the $MAPbI_3$ film on RF-ZnO decrease evidently. For both Al-ZnO and RF-

ZnO, there are no new peaks. As for S-ZnO, apart from the obviously decrease of spectrum intensity, we also observed the appearance of strong O-H stretching vibrations. The presence of hydroxyl group means that the $MAPbI_3$ has significantly decomposed. The hydroxyl group on the surface of ZnO is another reason for the decomposition of perovskites caused by the UV photocatalysis.[44] Hence, FTIR was used to determine the hydroxyl group residue on Al-ZnO, RF-ZnO and S-ZnO surface too. FTIR spectra of Al-ZnO, RF-ZnO and S-ZnO films are shown in Fig. 2(b). As can be seen, an evident broad peak between 3250 cm^{-1} and 3750 cm^{-1} can be observed in S-ZnO spectrum, while for Al-ZnO and RF-ZnO film, no evident peaks can be distinguished at the same position. This result indicates that there are fewer hydroxyl group residues on the RF-ZnO and Al-ZnO surfaces. The hydroxyl group residues mainly originated from chemical solution fabrication process of S-ZnO, which reacted with perovskite and enhanced the UV decomposition process. Fig. 2(c) and (d) exhibit the decomposition process of perovskite on different ZnO films. When the ZnO film without modification was used as ETM, due to the UV catalysis and reactive surface of ZnO film, the perovskite film can be decomposed in air under UV illumination. But once the ZnO surface was covered by the AlO_x interlayer, like shown in Fig. 2(d), the decomposition can be efficiently suppressed.

Ultraviolet-visible spectroscopy (UV-Vis) absorption spectra of $MAPbI_3$ film are used to exhibit details of the change of the optical properties during this process. Fig. 3(a) shows that the UV-Vis absorption of $MAPbI_3$ on Al-ZnO decreases only slightly in the range of 500-750 nm during the UV aging test. The optical band gap of perovskite keeps steady at about 760 nm. The missing absorption peak of PbI_2 demonstrates the high UV stability of $MAPbI_3$ on Al-ZnO.[50] The UV stability of $MAPbI_3$ on Al-ZnO is further confirmed by the photos in Fig. 3(a) that the color of $MAPbI_3$ is still dark brown after the aging test. As shown in Fig. 3(b), the absorption features of $MAPbI_3$ on RF-ZnO in the range of 500-750 nm decrease rapidly. The optical band gap of perovskite is not steady at 760 nm owing to perovskite decomposition in the UV aging process. At the same time, the background absorption of perovskite film increases over time during the aging test, which is because the large crystals formed by the decomposition of $MAPbI_3$.[51]

In addition, the color of the $MAPbI_3$ film changes from dark brown to pale yellow gradually because of the decomposition of $MAPbI_3$ induced by UV photocatalysis like shown in insets of Fig. 3(b). As shown in Fig. S6, the $MAPbI_3$ film on S-ZnO turns yellow in a short time owing to its much faster degradation. The dark brown color of $MAPbI_3$ film on Al-ZnO is stable under UV illumination. The result suggests that the environmental stability of $MAPbI_3$ films on Al-ZnO is drastically improved because of suppressing UV photocatalysis.

To further unravel the role of the AlO_X interlayer, the X-ray Photoelectron Spectrometer (XPS) spectrum are carried out on RF-ZnO and Al-ZnO films. As can be seen from the XPS spectra shown in Fig. 3(c), only two peaks located at binding energies of 1021.88 eV and 1044.98 eV are observed, corresponding to the $Zn_{2p3/2}$ and $Zn_{2p1/2}$, related to the Zn ion in the wurtzite ZnO. The XPS spectra of Al_{2p} peaks for Al-ZnO and RF-ZnO is shown in Fig. 3(d). There is no Al_{2p} peak in the XPS spectrum of RF-ZnO. As to Al-ZnO, a weak, but distinct peak for Al_{2p} located at binding energy of 74.68 eV corresponding to AlO_x is detected, which reveals the existence of alumina oxide. The results indicate the deposited Al reacts with O_2^- on the surface of ZnO and ambient O_2 to form ultrathin AlO_x layer on the ZnO surface, which is consisted with our assumptions.[45] AlO_x usually has much larger bandgap (about 8-9 eV) than ZnO (3.37 eV). Therefore, the UV light in solar spectrum is unable to activate the photocatalysis of AlO_x. Additionally, the AlO_x passivation inhibits ZnO surface trap states and decreases the oxygen vacancy concentration. As illustrated in Fig. 3(e), the O_{1s} peak in Al-ZnO can be deconvoluted into three peaks at 530.46 eV, 530.87 eV and 532.25 eV, respectively. The higher binding energy (532.25 eV) is related to the oxygen vacancy and chemisorbed oxygen on surface. Another peak appeared at 530.46 eV is associated with O atoms in the ZnO lattice. The peak at 530.87 eV corresponding to the O atoms bonded with Al. The integrated peak intensity ratio for Al-ZnO is 1.56 ($S_{530.46}/S_{532.25}$). As shown in Fig. 3(f), the O_{1s} in RF-ZnO can be deconvoluted into two peaks, corresponding to oxygen vacancy and chemisorbed oxygen at 532.06 eV and O atoms in the ZnO lattice at 530.52 eV. The integrated peak intensity ratio for these two peaks is 1.01 ($S_{530.52}/S_{532.06}$). The higher ratio in Al-ZnO reveals that AlO_x interlayer modification can efficiently reduce the amount of oxygen vacancies and chemisorbed oxygen. The AlO_x interlayer is thus favorable to suppress the UV instability of perovskite on ZnO surface in atmosphere.[36]

As shown in Fig. 4(a), the rapid decomposition of $MAPbI_3$ on S-ZnO and RF-ZnO is mainly owing to the photocatalysis of ZnO surface. The simulated sunlight used in the study contains about 3% UV light with wavelength less than 400 nm, which excites the photocatalytic activity of ZnO.[27,52] Under the illumination, electrons transit from the valence band to the conduction band to generate free electron-hole pairs. The photogenerated electrons and holes accumulate on the surface of ZnO and react with H_2O and O_2 adsorbed at the ZnO surface or in the ambient air, leading to formation of hydroxyl radicals (·OH) and O_2^-.[53,54] Both two groups show strong oxidizability and oxidize the $MAPbI_3$ materials on ZnO surface.

As the reaction continues, besides those from the reaction, H_2O in the air further aggravates the decomposition of $MAPbI_3$ and destroys the $MAPbI_3$ crystal structure.

H_2O is extremely unfavorable to the stability of $MAPbI_3$ due to the following reaction:[55]

$$4CH_3NH_3PbI_3 + 2H_2O \rightarrow (CH_3NH_3)_4PbI_6 \cdot 2H_2O + 3PbI_2$$

In addition, when $MAPbI_3$ contacts with ZnO, deprotonation reaction happens. The possible mechanism for this process is shown as follows:[44]

$$CH_3NH_3PbI_3 \rightarrow PbI_2 + CH_3NH_2 + HI$$

On the other hand, there are many oxygen vacancies on the surface of ZnO and the oxygen vacancies interact with O_2 and H_2O in air. Especially, a higher oxygen vacancy concentration is on the surface of S-ZnO due to the incomplete oxidation. In addition, chemicals and solvent remain on the surface of ZnO films are unavoidable for solution processes. As it is confirmed by the FTIR spectra in Fig. 2(b), the oxygen vacancies and chemical residues lead to a much higher concentration of surface hydroxyl. For S-ZnO, a broad peak is clearly shown at around 3500 cm^{-1}, corresponding to O-H stretching vibrations, i.e. the hydroxyl group. The improved quality of RF-ZnO causes absence of the broad peak ascribed to O-H stretches. The high concentration of hydroxyl on the surface of ZnO enhances the UV activity of ZnO surface.[44,45]

In order to intuitively verify the inference, photocatalytic properties of Al-ZnO, RF-ZnO and S-ZnO are evaluated by photocatalytic degradation of methylene blue (MB) under UV irradiation. The concentration evolution of MB solution during UV degradation can be monitored by measuring its characteristic absorption at 665 nm. As shown in Fig. 4(b), the absorption of MB solution on Al-ZnO has no significant change during 1 h UV exposure. Meanwhile, the absorption intensities of MB solution on RF-ZnO and S-ZnO decline rapidly under UV illumination, as exhibited in Fig. 4(c) and (d). MB itself is stable and cannot be degraded by UV light on its own. As a result, the absorption evolution, which is directly related to the concentration change, is mainly caused by the UV degradation introduced by ZnO. In addition, the degradation speed of MB on different ZnO films is shown in Fig. 4(e), where C_0 and C correspond to the initial concentration of MB and concentration of MB at different times, respectively. Decomposition rate of MB on S-ZnO is the fastest while the Al-ZnO shows the slowest decomposition rate. The stable characteristic absorption and slow degradation speed of MB show that the catalytic activity of the Al-ZnO is much lower than RF-ZnO and S-ZnO, which means that AlO_x modification is effective to inhibit the photo degradation and suppress the UV photocatalysis.

To gain further insights into the device degradation, the evolution of fundamental diode parameters of the Al-ZnO and RF-ZnO devices is analyzed during the UV aging process. The PSC is a non-ideal diode in darkness. Shockley diode equation explains the basic parameters of this diode as follows:[56]

$$J = \frac{1}{1 + \frac{R_S}{R_{SH}}}\left[J_0\left(\exp\left(\frac{q(V - JAR_S)}{nkT}\right) - 1\right) - \left(J_P - \frac{V}{R_{SH}A}\right)\right] \quad (1)$$

Where J is the current density of a diode, J_0 is the reverse saturated current density, J_P is photocurrent density, q is the electron charge, V is applied bias, R_S is series resistance, R_{SH} is shunt resistance, A is the area of device, n is the ideality factor of the junction, k is Boltzmann constant and T is Kelvin temperature. Considering the negligible R_S and huge R_{SH} in darkness, we derive an approximate relation of J, J_0, and n from eq (1), the equation is expressed as follows:

$$\ln J \approx \ln J_0 + \frac{qV}{nKT} \quad (2)$$

The natural logarithm plots of J versus V of RF-ZnO and Al-ZnO devices under dark conditions are shown in Fig. 5(a) and (b). The dark current of RF-ZnO PSC increases obviously over time and the dark current of Al-ZnO remains roughly stable and lower than the RF-ZnO device at the same time. The J_0 and n are estimated from the dark current curves by exponential fitting according to eq (2) (the temperature used here is 298K).[18] The results are shown in Fig. S7. As exhibited in the figure, prior to aging test, the ideal factor n and reverse saturated current density J_0 of Al-ZnO device is 1.71 and 2.01×10^{-11} mA/cm^2, and for RF-ZnO, the two factors are 1.84 and 1.2×10^{-10} mA/cm^2, respectively. Usually, for a high-performance heterojunction solar cell, the ideal factor generally is within the range of 1.3-2.[56] A bigger ideal factor means more non-radiative recombination (e.g. Shockley-Read-Hall (SRH) recombination via defects).[18] The reverse saturated current density J_0 relates to the recombination at the interface of $MAPbI_3$/ZnO. The AlO_x interlayer passivation of ZnO reduces the ideal factor of PSCs within the range of 1.3-2 and decreases the reverse saturated current density, indicating that the recombination is efficiently suppressed. As the aging process continues, n and J_0 of both types of devices increase with time. At the end of the aging test, the n and J_0 of the Al-ZnO device just slightly increase to 1.98 and 6.29×10^{-10} mA/cm^2, respectively. This reveals that the basic diode properties are almost unaffected, and the decomposition of $MAPbI_3$ is suppressed because of the AlO_x interlayer modification. Meanwhile, n and J_0 of PSCs based on RF-ZnO increase to 2.1 and 1.75×10^{-9} mA/cm^2 after UV exposure. The result confirms that recombination in RF-ZnO device increases, and $MAPbI_3$ on RF-ZnO continues to decompose under UV illumination.[57,58]

The introduction of AlO_x interlayer not only improves the long term stability, but also improves the perovskite film quality. Fig. 5(c) and (d) show the surface morphology of $MAPbI_3$ on RF-ZnO and Al-ZnO, respectively. The average grain size of $MAPbI_3$ on Al-ZnO is 384 nm, which is much larger than the average grain size of $MAPbI_3$ on RF-ZnO surface (310 nm). The grain size of $MAPbI_3$ on RF-ZnO obviously shows wider distribution as well. The cross section of FTO/Al-ZnO/perovskite shown in Fig. 5(g) reveals Al-ZnO is fully covered by a compact and well crystalized $MAPbI_3$

film. Fig. S8 shows that the grain size of $MAPbI_3$ on S-ZnO decreases to 200 nm, and the S-ZnO is not fully covered by the perovskite film. Per the previous report, the coverage evolution is mainly driven by the change of surface energy, and higher surface energy leads to lower coverage.[59] The S-ZnO shows much higher surface energy than RF-ZnO and Al-ZnO, because it is composed of the ZnO nanoparticles.[60] The poor coverage decreases the light absorption and result in shunt paths in perovskite film, which causes a drop in photovoltaic performance.

The X-ray diffraction (XRD) patterns of $MAPbI_3$ on Al-ZnO and RF-ZnO are shown in Fig 5(e). The absence of PbI_2 peaks of both samples means fully conversion of $MAPbI_3$ precursors. The XRD result of $MAPbI_3$ on Al-ZnO shows peaks corresponding to (100), (112), (211), (202), (220), (310), (312), (224), and (314) planes respectively. As for $MAPbI_3$ on RF-ZnO, XRD spectra show similar diffraction patterns except for the slightly decreased peak intensity and wider peak width ascribed to the decrease of grain size, which coincides with the scanning electron microscopy (SEM) result. The large grain size can decrease grain boundaries in $MAPbI_3$ films, resulting in the improvement of carrier transport and carrier extraction efficiency. The large perovskite grain is also favorable to the decrease of series resistance and the increase of FF. In addition, the large perovskite grains enhance light scattering and absorption, leading to the increase of J_{SC}.[3]

To further investigate the effects of the AlO_x interlayer on ZnO, we measured the I-V curves of unipolar devices with only electron charge carriers (FTO/ZnO/$MAPbI_3$/PCBM/Ag), as shown in inset of Fig. 5(f). The semilog plot of I-V curves indicates that current increases linearly with voltage at the low bias voltage region. At the higher bias voltage region, current increases at a much higher slope. The transition point is the ohmic to trap filled limit transition point (V_{TFL}) and related to the trap density (n_t) linearly. The value of V_{TFL} increases as electron traps. The trap-state is given by the following formula (3):[61]

$$V_{TFL} = \frac{en_tL^2}{2\varepsilon\varepsilon_0} \quad (3)$$

Where L is the thickness of $MAPbI_3$, ε and ε_0 is relative dielectric constant of $MAPbI_3$ (28.8) and vacuum permittivity.[62, 63] With the similar thickness of $MAPbI_3$, the n_t is proportional to V_{TFL}. As indicated from the I-V curves, the V_{TFL} of device based on Al-ZnO, RF-ZnO and S-ZnO are 0.24 V, 0.65 V and 0.7 V (Fig. S9). The results suggest trap density in $MAPbI_3$ film on Al-ZnO is drastically suppressed, and thus the performance of PSCs is improved. This result was further proved by the photoluminescence (PL) and time-resolved photoluminescence (TRPL) spectra shown in Fig. S10. Fig. S10(a) shows the steady state PL spectra of the perovskite on Al-ZnO, RF-ZnO and S-ZnO. The characteristic PL peak of perovskite at around 775 nm can be observed. The perovskite film on S-ZnO shows the highest PL intensity and the perovskite film on Al-ZnO shows the weakest. According to previous report, the electron extraction time in perovskite has been measured to be 0.4 ns.[64] However, the radiative recombination in perovskite occurs in tens to hundreds nanoseconds time scale,[65] as a result, the PL intensity is largely determined by the carrier extraction. Hence, the weakest PL intensity of perovskite on Al-ZnO indicated that the electron extraction efficiency and quality of perovskite film on Al-ZnO were higher than the perovskite films on RF-ZnO and S-ZnO. The TRPL spectra shown in Fig. S10(b) prove this result too. Compared with the S-ZnO and RF-ZnO samples, the Al-ZnO sample shows the shortest emission decay time, which indicates a good carrier extraction behavior of perovskite/Al-ZnO interface and high quality of perovskite film.

To further demonstrate the improved performance of PSCs based on Al-ZnO, we prepared two batches of planar PSCs based on Al-ZnO and RF-ZnO film. As shown in Fig. 6, the AlO_x interlayer modification increases the average PCE from 12.94% to 16.74%, the average V_{OC} from 1.017 V to 1.049 V, the average J_{SC} from to 19.27 mA/cm^2 to 21.44 mA/cm^2, and the average FF from 65.96% to 74.39%. Obviously, when Al-ZnO is used as the ETM, the solar cell performance is improved with high reproducibility. This result suggests that, after ZnO modified by AlO_x interlayer, the surface defects are efficiently passivated and recombination are suppressed. At the same time, the defect concentration in perovskite deposited on Al-ZnO is obviously decreased, and the carrier transport in the device is improved.

4. Conclusion

Planar PSCs based on the undoped ZnO ETM modified by an ultrathin AlO_x interlayer yield a high efficiency of 17.17%. The PCE is only reduced to 15.03% after 250 h continuously illumination in ambient environment. The AlO_x interlayer modification not only prevents ZnO induced photocatalysis, but also enhances the performance of PSCs. The results obtained from FTIR, UV-Vis absorption and diode parameter calculation demonstrate that the introduction of AlO_x interlayer on the surface of ZnO suppresses the defects and photocatalytic degradation, and hence improves the environmental instability of ZnO ETM based PSCs. Since the defects and environmental instability of ZnO can be effectively inhibited by the AlO_x interlayer, we provide a valid approach to overcome the barrier of use ZnO as ETM for high performance planar PSCs.

Acknowledgements

This work was supported by National Natural Science Foundation of China under Grant Nos. 61421002，61574029, and 61371046. This work was also partially supported by University of Kentucky. The manuscript was written through contributions of all

authors. All authors have given approval to the final version of the manuscript. The authors declare no competing financial interests.

Supporting Information

Figure S1. The transmittance of Al-ZnO and RF-ZnO films;

Figure S2. The J-V curve and EQE spectra of S-ZnO device;

Figure S3. The J-V curves of best performing PSC based on Al-ZnO measured by forward and reverse scans;

Figure S4. The steady state photocurrent output of the best performing PSC based on Al-ZnO;

Figure S5. The evolution of S-ZnO device photovoltaic parameters over time;

Figure S6. The absorption evolution of $MAPbI_3$ on S-ZnO and photos of the perovskite film;

Figure S7. The evolution of ideal factor and reverse saturated current density over time;

Figure S8. The SEM of surface and cross section of $MAPbI_3$ on S-ZnO;

Figure S9. The V_{TFL} of the electron-only device based on S-ZnO;

Figure S10. The PL and TRPL spectra of perovskite on Al-ZnO, RF-ZnO and S-ZnO;

Table S1. Detail photovoltaic data of Al-ZnO, RF-ZnO and S-ZnO devices before and after aging.

References

1 A. Kojima, K. Teshima, Y. Shirai and T. Miyasaka, *J. Am. Chem. Soc.*, 2009, **131**, 6050-6051.

2 J. Burschka, N. Pellet, S. J. Moon, R. Humphry-Baker, P. Gao, M. K. Nazeeruddin and M. Gratzel, *Nature*, 2013, **499**, 316-319.

3 J. H. Im, I. H. Jang, N. Pellet, M. Gratzel and N. G. Park, *Nat. Nanotechnol.*, 2014, **9**, 927-932.

4 N. J. Jeon, J. H. Noh, W. S. Yang, Y. C. Kim, S. Ryu, J. Seo and S. I. Seok, *Nature*, 2015, **517**, 476-480.

5 H. Li, Shibin. Li, Y. Wang, H. Sarvari, Peng. Zhang, M. Wang and Z. Chen, *Solar Energy*, 2016, **126**, 243-251.

6 Y. Wang, Shibin. Li, Peng. Zhang, D. Liu, X. Gu, H. Sarvari, Z. Ye, J. Wu, Z. Wang and Z. D. Chen, *Nanoscale*, 2016, **8**, 19654-19661.

7 H. S. Kim, C. R. Lee, J. H. Im, K. B. Lee, T. Moehl, A. Marchioro, S. J. Moon, R. Humphry-Baker, J. H. Yum, J. E. Moser, M. Gratzel and N. G. Park, *Sci. Rep.*, 2012, **2**, 591.

8 J. H. Im, C. R. Lee, J. W. Lee, S. W. Park and N. G. Park, *Nanoscale*, 2011, **3**, 4088-4093.

9 M. M. Lee, J. Teuscher, T. Miyasaka, T. N. Murakami and H. J. Snaith, *Science*, 2012, **338**, 643-647.

10 M. Wang, Shibin. Li, Peng. Zhang, Y. Wang, H. Li and Z. Chen, *Chem. Phys. Lett.*, 2015, **639**, 283-288.

11 H. Chen, Z. Wei, H. He, X. Zheng, K. S. Wong and S. Yang, *Adv. Energy Mater.*, 2016, **8**, 1502087.

12 N. J. Jeon, J. H. Noh, Y. C. Kim, W. S. Yang, S. Ryu and S. I. Seok, *Nature materials*, 2014, **13**, 897-903.

13 Y. Rong, Z. Tang, Y. Zhao, X. Zhong, S. Venkatesan, H. Graham, M. Patton, Y. Jing, A. M. Guloy and Y. Yao, *Nanoscale*, 2015, **7**, 10595-10599.

14 M. Liu, M. B. Johnston and H. J. Snaith, *Nature*, 2013, **501**, 395-398.

15 P. Luo, Z. Liu, W. Xia, C. Yuan, J. Cheng and Y. Lu, *ACS Appl. Mater. Interfaces*, 2015, **7**, 2708-2714.

16 W. S. Yang, J. H. Noh, N. J. Jeon, Y. C. Kim, S. Ryu, J. Seo and S. I. Seok, *Science*, 2015, **348**, 1234-1237.

17 F. Giordano, A. Abate, J. P. Correa Baena, M. Saliba, T. Matsui, S. H. Im, S. M. Zakeeruddin, M. K. Nazeeruddin, A. Hagfeldt and M. Graetzel, *Nat. Commun.*, 2016, **7**, 10379.

18 D. Bi, W. Tress, M. I. Dar, P. Gao, J. Luo, C. Renevier, K. Schenk, A. Abate, F. Giordano, J. P. Correa Baena, J. D. Decoppet, S. M. Zakeeruddin, M. K. Nazeeruddin, M. Gratzel and A. Hagfeldt, *Sci. Adv.*, 2016, **2**, e1501170.

19 X. Li, D. Bi, C. Yi, J. D. Decoppet, J. Luo, S. M. Zakeeruddin, A. Hagfeldt and M. Gratzel, *Science*, 2016, **353**, 58-62.

20 T. M. Koh, K. Fu, Y. Fang, S. Chen, T. C. Sum, N. Mathews, S. G. Mhaisalkar, P. P. Boix and T. Baikie, *J. Phys. Chem. C*, 2014, **118**, 16458-16462.

21 A. Amat, E. Mosconi, E. Ronca, C. Quarti, P. Umari, M. K. Nazeeruddin, M. Gratzel and F. De Angelis, *Nano Lett.*, 2014, **14**, 3608-3616.

22 P. Luo, W. Xia, S. Zhou, L. Sun, J. Cheng, C. Xu and Y. Lu, *J. Phys. Chem. Lett.*, 2016, **7**, 3603-3608.

23 A. Swarnkar, A. R. Marshall, E. M. Sanehira, B. D. Chernomordik, D. T. Moore, J. A. Christians, T. Chakrabarti and J. M. Luther, *Science*, 2016, **354**, 92-95.

24 G. E. Eperon, G. M. Paternò, R. J. Sutton, A. Zampetti, A. A. Haghighirad, F. Cacialli and H. J. Snaith, *J. Mater. Chem. A*, 2015, **3**, 19688-19695.

25 M. Saliba, T. Matsui, J. Y. Seo, K. Domanski, J. P. Correa-Baena, M. K. Nazeeruddin, S. M. Zakeeruddin, W. Tress, A. Abate, A. Hagfeldt and M. Gratzel, *Energy Environ. Sci*, 2016, **9**, 1989-1997.

26 C. Klingshirn, J. Fallert, H. Zhou, J. Sartor, C. Thiele, F. Maier‐Flaig, D. Schneider and H. Kalt, *Physica. Status Solidi (b)*, 2010, **247**, 1424-1447.

27 Ü. Özgür, Y. I. Alivov, C. Liu, A. Teke, M. Reshchikov, S. Doğan, V. Avrutin, S.-J. Cho and H. Morkoc, *J. Appl. Phys.*, 2005, **98**, 11.

28 U. Diebold, *Surface science reports*, 2003, **48**, 53-229.

29 M. Law, L. E. Greene, J. C. Johnson, R. Saykally and P. Yang, *Nat. Mater.*, 2005, **4**, 455-459.

30 D. Liu and T. L. Kelly, *Nature Photon*, 2013, **8**, 133-138.

31 D. Bi, G. Boschloo, S. Schwarzmuller, L. Yang, E. M. Johansson and A. Hagfeldt, *Nanoscale*, 2013, **5**, 11686-11691.

32 D.-Y. Son, J.-H. Im, H.-S. Kim and N.-G. Park, *J. Phys. Chem. C*, 2014, **118**, 16567-16573.

33 K. Mahmood, B. S. Swain and A. Amassian, *Adv. Energy Mater.*, 2015, **5**, 17.

34 Shibin. Li, Peng. Zhang, Y. Wang, H. Sarvari, D. Liu, J. Wu, Y. Yang, Z. Wang and Z. D. Chen, *Nano Res.*, 2016, 1-12.

35 Shibin. Li, Peng. Zhang, H. Chen, Y. Wang, D. Liu, J. Wu, H. Sarvari and Z. D. Chen, *J. Power Sources*, 2017, **342**, 990-997.

36 Z.-L. Tseng, C.-H. Chiang, S.-H. Chang and C.-G. Wu, *Nano Energy*, 2016, **28**, 311-318.

37 J. Dong, Y. Zhao, J. Shi, H. Wei, J. Xiao, X. Xu, J. Luo, J. Xu, D. Li, Y. Luo and Q. Meng, *Chem. Commun.*, 2014, **50**, 13381-13384.

38 J. You, L. Meng, T.-B. Song, T.-F. Guo, Y. Yang, W.-H. Chang, Z. Hong, H. Chen, H. Zhou, Q. Chen, Y. Liu, N. De Marco and Y. Yang, *Nat. Nanotechnol.*, 2015, **11**, 75-81.

39 X. Zhao, H. Shen, Y. Zhang, X. Li, X. Zhao, M. Tai, J. Li, J. Li, X. Li and H. Lin, *ACS Appl. Mater. Interfaces*, 2016, **8**, 7826-7833.

40 I. S. Kim, D. H. Cao, D. B. Buchholz, J. D. Emery, O. K. Farha, J. T. Hupp, M. G. Kanatzidis and A. B. Martinson, *Nano Lett.*, 2016, **16**, 7786-7790.

41 T. Leijtens, G. E. Eperon, S. Pathak, A. Abate, M. M. Lee and H. J. Snaith, *Nat. Commun.*, 2013, **4**.

42 Y. Li, J. K. Cooper, W. Liu, C. M. Sutter-Fella, M. Amani, J. W. Beeman, A. Javey, J. W. Ager, Y. Liu, F. M. Toma and I. D. Sharp, *Nat. Commun.*, 2016, **7**, 12446.

43 W. Li, W. Zhang, S. Van Reenen, R. J. Sutton, J. Fan, A. A. Haghighirad, M. B. Johnston, L. Wang and H. J. Snaith, *Energy Environ. Sci.*, 2016, **9**, 490-498.

44 Y. Cheng, Q. D. Yang, J. Xiao, Q. Xue, H. W. Li, Z. Guan, H. L. Yip and S. W. Tsang, *ACS Appl. Mater. Interfaces*, 2015, **7**, 19986-19993.

45 J. Yang, B. D. Siempelkamp, E. Mosconi, F. De Angelis and T. L. Kelly, *Chem. Mater.*, 2015, **27**, 4229-4236.

46 Z. Kam, X. Wang, J. Zhang and J. Wu, *ACS Appl. Mater. Interfaces*, 2015, **7**, 1608-1615.

47 N. Ahn, D. Y. Son, I. H. Jang, S. M. Kang, M. Choi and N. G. Park, *J. Am. Chem. Soc.*, 2015, **137**, 8696-8699.

48 J. Idigoras, A. Todinova, J. R. Sanchez-Valencia, A. Barranco, A. Borras and J. A. Anta, *Phys. Chem. Chem. Phys.*, 2016, **18**, 13583-13590.

49 A. Abate, T. Leijtens, S. Pathak, J. Teuscher, R. Avolio, M. E. Errico, J. Kirkpatrik, J. M. Ball, P. Docampo, I. McPherson and H. J. Snaith, *Phys. Chem. Chem. Phys.*, 2013, **15**, 2572-2579.

50 Y. Wu, A. Islam, X. Yang, C. Qin, J. Liu, K. Zhang, W. Peng and L. Han, *Energy Environ. Sci.*, 2014, **7**, 2934.

51 J. Yang, B. D. Siempelkamp, D. Liu and T. L. Kelly, *ACS nano*, 2015, **9**, 1955-1963.

52 D. Myers, S. Kurtz, K. Emery, C. Whitaker and T. Townsend, in *Photovoltaic Specialists Conference, 2000. Conference Record of the Twenty-Eighth IEEE*, IEEE, 2000, pp. 1202-1205.

53 N. Daneshvar, M. Rabbani, N. Modirshahla and M. Behnajady, *J photoch photobio A*, 2004, **168**, 39-45.

54 M. Behnajady, N. Modirshahla and R. Hamzavi, *J Hazard Mater*, 2006, **133**, 226-232.

55 A. M. A. Leguy, Y. Hu, M. Campoy-Quiles, M. I. Alonso, O. J. Weber, P. Azarhoosh, M. van Schilfgaarde, M. T. Weller, T. Bein, J. Nelson, P. Docampo and P. R. F. Barnes, *Chem. Mater.*, 2015, **27**, 3397-3407.

56 B. Kippelen and J.-L. Brédas, *Energy Environ. Sci.*, 2009, **2**, 251-261.

57 J. Dong, X. Xu, J.-J. Shi, D.-M. Li, Y.-H. Luo, Q.-B. Meng and Q. Chen, *Chin. Phys. Lett.*, 2015, **32**, 078401.

58 D. Zhao, M. Sexton, H. Y. Park, G. Baure, J. C. Nino and F. So, *Adv. Energy Mater.*, 2015, **5**.

59 G. E. Eperon, V. M. Burlakov, P. Docampo, A. Goriely and H. J. Snaith, *Adv. Funct. Mater.*, 2014, **24**, 151-157.

60 Z.-Y. Zhou, N. Tian, J.-T. Li, I. Broadwell and S.-G. Sun, *Chem. Soc. Rev.*, 2011, **40**, 4167-4185.

61 D. Yang, X. Zhou, R. Yang, Z. Yang, W. Yu, X. Wang, C. Li, S. Liu and R. P. H. Chang, *Energy Environ. Sci.*, 2016, **9**, 3071-3078.

62 H. S. Jung and N. G. Park, *Small*, 2015, **11**, 10-25.

63 D. Zhao, C. Zhang, H. Kim and L. J. Guo, *Adv. Energy Mater.*, 2015, **5**.

64 Z. L. Zhu, J. Ma, Z. L. Wang, C. Mu, Z. Fan, L. L. Du, Y. Bai, L. Z. Fan, H. Yan, D. L. Phillips, S. H. Yang, *J. Am. Chem. Soc.*, 2014, **136**, 3760.

65 N. Sakai, S. Pathak, H. W. Chen, A. A. Haghighirad, S. D. Stranks, T. Miyasaka, H. J. Snaith, *J. Mater. Chem. A*, 2016, **4**, 4464.

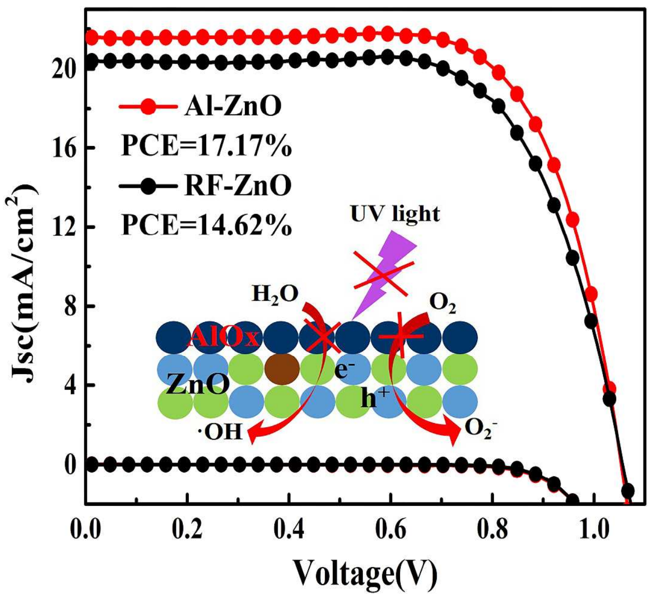

Al modified compact ZnO films based planar PSCs exhibit high environmental stability and UV resistance.